Radiative and climate effects of stratospheric sulfur geoengineering using seasonally varying injection areas

Anton Laakso[1,2], Hannele Korhonen[3], Sami Romakkaniemi[1], Harri Kokkola[1]

[1]Finnish Meteorological Institute, Atmospheric Research Centre of Eastern Finland, Kuopio, FI-70200, Finland
[2]Department of Soil, Water and Climate, University of Minnesota, Twin Cities, St. Paul, MN-55108, Minnesota, USA
[3]Finnish Meteorological Institute, Climate Research, Helsinki, FI-00100, Finland

Correspondence to: Anton Laakso (anton.laakso@fmi.fi)

Abstract. Stratospheric sulfur injections have often been suggested as a cost effective geoengineering method to prevent or slow down global warming. In geoengineering studies these injections are commonly targeted to the equator, where the intensity of the solar radiation is highest. However, it may not be the most optimal aerosol injection strategy because the radiative forcing concentrating over the equator decreases the meridional temperature gradient. In this study we employ alternative aerosol injection scenarios to investigate if the resulting radiative forcing can be optimized to be zonally more uniform without decreasing the global efficacy. We used a global aerosol-climate model together with an Earth system model to study the radiative and climate effects of stratospheric sulfur injection scenarios with different injection areas. According to our simulations, varying the SO_2 injection area seasonally would result in a similar global mean cooling effect as injecting SO_2 to the equator, but with a more uniform zonal distribution of shortwave radiative forcing. Compared to the case of equatorial injections, in the optimized injection scenario where the maximum sulfur production from injected SO_2 followed the maximum of solar radiation, the shortwave radiative forcing decreased by 27% over the equator (between the latitudes between 20° N and 20° S) and increased by 15% over higher latitudes. Compared to the continuous injections to equator, in summer months the radiative forcing was increased by 17% and 14% and winter months decreased by -14% and -16% at northern and southern hemispheres respectively. However, these forcings do not translate into very significant changes in temperatures. Based on ESM simulations, changes in forcing would lead only to 0.05 K warmer winters and 0.05 K cooler summers at the northern hemisphere which is roughly 3 % of the cooling resulted from solar radiation management scenarios studied here. At the same time the meridional temperature gradient was better maintained.

1 Introduction

Solar radiation management (SRM) by increasing atmospheric aerosol particle concentration has been shown to have potential to counteract at least some of the ongoing global warming, and has therefore been considered a possible option to reduce the risks of climate change caused by increased greenhouse gas concentration in the atmosphere (Royal Society, 2009). One of the proposed methods is to produce sulfate particles into the stratosphere, where they efficiently reflect solar radiation back to space and thus cool the surface climate. It has been suggested that sulfur for geoengineering purposes could be injected as SO_2

which is oxidized to H_2SO_4 and subsequently forms sulfate particles (Kravitz et al., 2013a; Royal Society, 2009). Because of the stability of the stratosphere and the lack of efficient removal mechanisms, the stratospheric lifetime of sulfate particles is 1-2 years which would lead to longer lasting cooling than aerosol emissions at surface.

5   Most previous modelling studies have investigated scenarios which inject sulfur along or close to the equator. This choice of injection region is well justified because the equator, on the average, receives the highest levels of solar radiation. In addition, the stratospheric circulation transports particles efficiently from the equator around the global atmosphere (Robock et al., 2008). However it has been found in several studies that preventing greenhouse gas (GHG) induced warming by equatorial injections of sulfur lead to overcooling of the tropics and undercooling of the polar regions, compared to the global mean

10   decrease in temperature (Aswathy et al., 2015; Jones et al., 2010; Jones et al., 2016; McCuster et al., 2012; Yu et al., 2015). This would also lead to reduced meridional temperature gradient, which, for example, could reduce midlatitude precipitation (Schmidt et al., 2012). Therefore, it is worth investigating whether different spatial injection patterns could lead to more uniform cooling around the globe.

15   The previous research on this topic has shown that the temperature response would indeed be zonally more uniform if radiative forcing were concentrated to the extra-tropics. These studies have, however, used either a reduced solar constant (MacMartin et al., 2012) or prescribed aerosol fields (Modak and Bala, 2014) to approximate the climate impacts of stratospheric sulfur injections. While such simplified scenarios are useful for studying climate response in idealized scenarios and easily be implemented to various climate models, the applied radiative forcing does not necessarily correspond to the forcing that would

20   result from actual stratospheric injections of SO_2. This is because a reduced solar constant or prescribed aerosol fields do not account for the transport of gas and particulate phase sulfur in the stratosphere, which impacts the spatial distribution of the sulfate particles, nor aerosol microphysics, which can significantly affect the radiative properties and the lifetime of the aerosol population (Heckendorn et al., 2009). Thus, climate model studies using description of aerosol microphysics and sulfur chemistry are required for more realistic simulations of stratospheric sulfur injection strategies. The only studies of this kind

25   to date (Robock et al., 2008; Volodin et al., 2011) injected sulfur to high latitudes which lead to significantly smaller radiative forcing than equatorial injections.

In this study, we have investigated injection scenarios that aim to produce a geographically more even radiative forcing pattern than equatorial sulfur injections, while still maintaining a high global mean forcing. Such scenarios are sought via seasonally

30   varying injection areas in which the target area follows the maximum solar intensity with different time lags. These scenarios are compared to more commonly used strategies with fixed injection areas. The simulations are done in two steps. First we use the global aerosol-climate model ECHAM-HAMMOZ to investigate the radiative forcing from the zonally different injection areas and to define aerosols fields. Second, the global and regional temperature and precipitation responses are studied using the coupled climate-ocean model MPI-ESM.

2 Methods

2.1 Simulated SRM scenarios

Eight zonally different sulfur injection strategies were simulated. In all of these scenarios 5 Tg(S)/yr of gaseous SO_2 was injected to the stratosphere at the height of 20 km and to a 20 degree wide latitude band specified below (2 bands in one of the simulated scenarios).

2.1.1 Fixed injection areas

In three of the studied injection scenarios, the injection area remained fixed throughout the year. In scenario **EQ**, sulfur was injected to the equator between latitudes 10° N and 10° S (Figure 1a). This injection strategy corresponds to the injection scenarios in most previous studies, although they have used different widths for the injection area (Heckendorn et al., 2009; Jones et al., 2016; Niemeier et al., 2011; Pierce et al., 2010; Pope et al., 2012; Tilmes et al., 2015). In **NH** scenario sulfur was injected only to the northern hemisphere between latitudes 10° N and 30° N (Figure 1b). In scenario **NHSH** 2.5 Tg(S)/yr sulfur was injected to the northern hemisphere between latitudes 10° N and 30° N and 2.5 Tg(S)/yr to the southern hemisphere between latitudes 10° S and 30° S (Figure 1c) to reduce the overcooling in the tropics inherent to equatorial injections and aiming at reducing the change in the meridional temperature gradient compared to the scenario **EQ**. However, **NH** and **NHSH** are expected to result in a smaller global cooling effect than **EQ** because sulfur is injected to latitudes where the annual mean solar radiation is smaller than over the equator.

2.1.2 Seasonally changing injection areas

In addition, five scenarios where the sulfate injection area is varied throughout the year were simulated. In four of these scenarios, the 20-degree wide sulfur injection area changed between the latitudes from 30° S to 30° N in different phases. In the **p0** scenario, the injection area was set to follow the maximum intensity of solar radiation (Fig. 2). Therefore, the sulfur injection area is in its northernmost position (30° N to 10° N) in June coinciding with the location of the **NH** scenario. In March and September, the center of the injection area is in the equator, thus coinciding with the injection area of **EQ** scenario. The injections are at their southernmost location between 30° S to 10° S in December.

However, sulfur injected as SO_2 takes weeks to months before it is oxidized and forms large enough particles to reflect solar radiation efficiently. Thus to obtain maximum aerosol forcing, one strategy could be to inject sulfur before the intensity of solar radiation has reached its maximum value at the injection latitude, thus leaving time for oxidation and particle growth. To test this strategy, we repeated **p0** with different temporal phases of the injection area change. In the **p2** scenario, the northernmost injection area is reached in April, two months earlier than in the **p0** scenario. In the **p4** scenario, the northernmost injection area is reached in February and in **p6** in December. Injection areas in these scenarios are presented in figure 2. Based on model simulations in Laakso et al. (2016), in the case of Pinatubo eruption, 75% of the erupted SO_2 was oxidized after the

first two months from the eruption. In these simulations, the global mean radiative forcing of aerosols was also at its largest roughly at the same time. Thus, it could be expected that scenario **p2** would lead to stronger global mean radiative forcing than the other scenarios studied. To test the impact of concentrating radiative forcing to even higher latitudes, simulation **p2** was repeated so that the latitude range for the monthly-shifting injection area was wider. In this **p2w** scenario, the phase and the injection areas is as wide as in **p2** (20° in latitudinal direction), but the northernmost location of the injection area in April is between 40° N and 20° N and southernmost in October between 20° S and 40° S.

2.2 Model description

As explained above, the model simulations were done in two steps: First, the different injection strategies described in sect. 2.1 were simulated with the global aerosol-climate model ECHAM-HAMMOZ that contains an explicit description of SO_2 oxidation chemistry as well as aerosol microphysics. These simulations were used to calculate the radiative forcing resulting from the stratospheric injections, as well as to provide optical properties of stratospheric aerosol fields for the MPI-ESM simulations in step two. Second, the coupled earth system model MPI-ESM was used to the simulate temperature and precipitation effects of stratospheric sulfur injection strategies against the Representative Concentration Pathway 4.5 (RCP4.5, Moss et al., 2010; van Vuuren et al., 2011). Two step approach was selected because MPI-ESM does not include a prognostic calculation of aerosol processes in its current configuration.

2.2.1 Defining aerosol fields using ECHAM-HAMMOZ

As mentioned above, the radiative properties of aerosol fields resulting from the 5 Tg(S)/yr stratospheric sulfur injections were defined by using the global aerosol-climate model ECHAM-HAMMOZ (MAECHAM6.1-HAM2.2-SALSA). Nine-year long simulations were performed for each of the scenarios. The simulations started in conditions without SRM and included a two-year ramp-up period where SO_2 injection has started (5 Tg(S)/yr). This two-year ramp-up was long enough for the formation of a steady-state stratospheric sulfate field where averagely same amount of sulfur is removed from atmosphere than was injected. The ramp-up period was followed by a five-year steady-state period during which the sulfur field was maintained by continuous 5 Tg(S)/yr injections. Furthermore, two additional years were ran for simulate suspension of solar radiation management. In the beginning of this ramp-down period sulfur injections are suspended. After two years, sulfate particles from the injections are removed from the atmosphere.

For further analysis, the radiative forcings and stratospheric sulfur burdens were calculated as five-year mean values over the steady-state period and compared to the CTRL simulation which included only standard tropospheric emissions (see below). Furthermore, for the climate simulations, the radiative properties of the aerosol fields were calculated and implemented in MPI-ESM as monthly means.

Simulations were performed with a T63L47 resolution, which corresponds approximately to a 1.9° x 1.9° horizontal grid and in which the atmosphere is divided into 47 height levels reaching up to ~80 km. The aerosol module HAM is coupled interactively to ECHAM and includes an explicit sectional aerosol scheme SALSA (Bergman et al., 2012; Kokkola et al., 2009; Laakso et al., 2016), which calculates the microphysical processes of nucleation, condensation, coagulation and

5   hydration. In the SALSA configuration used, aerosols are described by aerosol number and volume size distributions with 10 size sections for internally and 7 size sections for externally mixed particles (see Laakso et al., (2016) for details). The HAM module calculates aerosol emissions, removal, gas and liquid phase chemistry, and radiative properties for the major global aerosol compounds of sulfate, organic carbon, black carbon, sea salt and mineral dust. Aerocom II tropospheric emissions for year 2010 were used in all simulations (Dentener et al., 2006). Simulations were carried out using a free running setup to

10   include the dynamical feedback resulting from the additional heating due to absorption radiation by the injected aerosols. The simulations were done using CMIP5 AMIP2 climatological sea surface temperatures and sea ice distributions which are derived as a mean values between years 1979-2008 (Taylor et al., 2008).

2.2.2 Simulating climate effects using MPI-ESM

15   To study the climate effects of the different stratospheric sulfur injection scenarios, we used the Max Planck Institute's Earth system model (MPI-ESM) (Giorgetta et al., 2013). The model is a state-of-the-art coupled three-dimensional atmosphere-ocean-land surface model. The model consists of the atmospheric component ECHAM6.1 (Stevens et al., 2013) which is coupled to the Max Planck Institute Ocean Model (MPIOM) (Junglaus et al., 2012). MPI-ESM also includes the land model JSBACH (Reich et al., 2013) and the ocean biochemistry model HAMOCC (Ilyina et al., 2013).

20

In this study, global fields of radiative properties of stratospheric aerosol from ECHAM-HAMMOZ simulations were implemented to MPI-ESM. The aerosol optical depth, single scattering albedo and asymmetry factor for the stratospheric aerosol field were first calculated for 30 wavelength bands using ECHAM-HAMMOZ and then used as an input for MPI-ESM. The implementation method used here is an improvement to that presented by Laakso et al. (2016), where the aerosol

25   radiative properties in MPI-ESM were calculated based on a single modal size distribution with a fixed mode width and monthly mean values of aerosol effective radius and aerosol optical depth (AOD) at 550 nm resulting from simulations with ECHAM-HAMMOZ. Thus particle size distribution in MPI-ESM was described by single mode, which did not correspond sectional size distribution in ECHAM-HAMMOZ. This led to slightly different aerosol radiative forcing in MPI-ESM than what was calculated by ECHAM-HAMMOZ (Laakso et al., 2016). In current study the only difference in the stratospheric

30   aerosol radiative properties between ECHAM-HAMMOZ and MPI-ESM in this study is that in MPI-ESM simulations the stratospheric aerosol fields are described as zonal monthly mean values. This difference is not expected to affect the results significantly; however, the chosen approach keeps the size of the aerosol input files for MPI-ESM manageable. To describe the properties of the tropospheric aerosol in MPI-ESM, we used the tropospheric aerosol climatology of Kinne et al., 2013 in all simulations.

Climate simulations with MPI-ESM were based on the Geoengineering Model Intercomparison Project (GeoMIP) G4 scenario (Kravitz et al., 2011, Kravitz et al., 2013a); however, in our study 5 Tg(S)/yr is injected instead of 2.5 Tg (S)/yr to get stronger climate signal. As with GeoMIP, we started our simulations from year 2010 and continued until 2100. The baseline scenario with no SRM followed the RCP4.5 scenario. All SRM scenarios also included the RCP4.5 tropospheric emissions but also additional stratospheric sulfur injections starting in the year 2020. The sulfur injections were applied for 50 years and then suspended. After that, the simulations were continued for 30 years until year 2100 to simulated termination effect of geoengineering (Jones et al., 2013; Kravitz et al., 2011). Growing sulfur field in the two-year ramp-up period simulated by ECHAM-HAMMOZ was used in MPI-ESM for years 2020-2021. The ramp-down period sulfur field, when sulfur injections are suspended and sulfate particles are removed from atmosphere was used for years 2070-2071. Between the ramp-up and ramp-down periods (2022-2070) steady-state stratospheric sulfur field from 5 Tg (S)/yr injection from simulations with ECHAM-HAMMOZ were used.

3 Results

3.1 Radiative forcings of alternative injection scenarios – Atmosphere-only simulations using ECHAM-HAMMOZ

Table 1 shows the global SO_2 and sulfate burdens and the global mean all-sky short-wave (SW) radiative forcing in the studied sulfur injection scenarios. The baseline **EQ** scenario leads to an all-sky SW radiative forcing of -3.72 W/m². As expected, both **NH** and **NHSH** scenarios give clearly smaller radiative impacts (-3.21 and -3.30 W/m², respectively) than **EQ**, since in these two scenarios sulfur is injected to an area where solar intensity is on average weaker (Robock et al., 2008). Further contributing to the smaller forcing in **NH** and **NHSH** is the fact that the lifetime of stratospheric sulfur is longer when injected to the equator (Robock et al., 2008).

It is interesting to note that **NH** and **NHSH** produce somewhat different global mean SW radiative forcings as well as stratospheric SO_2 and sulfate burdens even though in both cases the sulfur is injected to regions with equal distances from the Equator. The difference between these two scenarios is that in scenario **NH**, the same amount of sulfur is injected to a smaller total area than in **NHSH**. Previous research has shown that higher injections per unit volume lead to relatively larger particles, which in turn leads to relatively shorter lifetime of particles in the atmosphere (Heckendorn et al., 2009; English et al., 2012; Niemeier et al., 2011). The forcing in **NH** scenario is further reduced compared to **NHSH** by the fact that the Earth's albedo is higher in the northern than in the southern hemisphere.

The global burdens and mean forcings in the scenarios with seasonally changing sulfur injection area (**p0**, **p2**, **p4**, **p6**) are quite close to those in the **EQ** scenario (Table 1). However, it is noteworthy that out of all the scenarios the largest radiative forcing of -3.82 W/m² (i.e. 0.1 W/ m² larger than in **EQ**) is simulated in scenario **p2**. When the injection area is varied throughout the

year in a well-timed phase, the reflective sulfate particles are on the average concentrated to latitudes with larger solar intensity than if sulfur is injected only to the equator (**EQ**). It can be expected that the difference in the efficiency between scenarios **EQ** and **p2** would increase even more if a larger amount of sulfur were injected, because of a sub-linear correlation between the amount of annual sulfur injections and radiative forcing (Heckendorn et al., 2009). Such losses are slower when the injection area is varied and thus injections per unit volume of air is smaller, and thus more newly formed particles survive to become large enough to scatter radiation efficiently.

Based on the scenarios used here, to achieve maximum aerosol forcing the varying sulfur injection area should reach its northernmost location two months (April) earlier (**p2**) than the solar radiation reaches its maximum (June). This way, the formed particles from SO_2 injection reach the optimal size at the time of maximum solar radiation. On the other hand, in **p0** and **p6** scenarios the seasonality of solar radiation intensity and its impacts on the seasonality of hydroxyl radical (OH) concentration lead to a lower global forcing than in most other scenarios (**EQ**, **p2**, **p4**, **p2w**). This is because OH is the main oxidant that converts SO_2 to sulfuric acid (H_2SO_4) which together with H_2O molecules nucleates and grows the stratospheric aerosol particles. In the **p0** scenario, the SO_2 injection area follows the area which receives the highest amount of solar radiation. These latitudes have high OH concentration which leads to faster oxidation than in other scenarios, as can be seen from the smallest SO_2 burden in Table 1. However, it takes a couple of months before the formed particles have grown large enough to reflect solar radiation effectively, and by the time this happens, the solar intensity has already decreased at the latitudes where the particulate sulfur burden has increased the most. On the other hand, in **p6** sulfur is injected always during the months when the injection region experiences its lowest annual solar radiation. This leads to a relatively slow oxidation rate, as can be seen from the large SO_2 burden. However, because of the lifetime of sulfate particles is over one year, most of the injected sulfur is still in the atmosphere in the summer around 6 months after the injection, and thus the global mean radiative forcing is not significantly smaller than in the other scenarios. In addition, here sulfur is injected in all **p0**, **p2**, **p4** and **p6** scenarios to the low latitudes (between 30° N and 30° S) which receive high solar radiation throughout the year. Thus considerably large differences in the global yearly mean radiative forcing between the scenarios are not expected.

Finally, in **p2w** the injection area changes between 40° N and 40° S instead of 30° N and 30° S. Because sulfur is injected at a larger distance from the equator than in **p2**, the global mean all-sky shortwave radiative forcing is 3% (0.1 W/m²) smaller than in **p2** (Table 1). While the all-sky forcing is as large as in **EQ** (Table 1), it is noteworthy that the clear-sky forcing is 0.16 W/m² larger in scenario **p2w** than scenario **EQ** (5.76 W/m² and 5.60 W/m², respectively). This is because in scenario **p2w** more sulfur resides in the mid-latitudes (40° - 60°) where the cloud cover is larger than in the low latitudes and therefore the original albedo is larger. This decreases the all-sky radiative forcing of **p2w** compared to **EQ**.

Overall the results show that extending the injection area to the mid-latitudes for a part of the year can, in terms of the global forcing, be as effective as the injections to the equator if the injection area is changed in a certain phase. However, the zonal differences between these two injection strategies can be very different, as will be illustrated in the following.

5   Figure 3 shows the five-year zonal mean shortwave radiative forcing in **EQ**, **NH**, **NHSH**, **p2** and **p2w** scenarios. As expected, scenario **EQ** (black line) leads to the strongest radiative forcing at the equator; however, outside the tropics the forcing declines fast (**EQ**). In the **p2** (purple solid line) and **p2w** (purple dashed line) scenarios the forcing is distributed much more evenly throughout the tropics and the midlatitudes. Compared to **EQ**, **p2** shows 7% lower mean forcing between 20° N and 20° S, but 10% larger forcing in higher latitudes. The difference between **p2w** and **EQ** is even larger: 27% between 20° S and 20° N and

10   15% in higher latitudes. Thus these results show that by varying the injection area it would be possible to obtain a more evenly distributed zonal forcing or even concentrate the maximum forcing to mid-latitudes, while achieving similar or even larger global mean radiative forcing than in scenario **EQ**. This could prevent some of the decrease of the meridional temperature gradient due to geoengineering and GHG induced warming.

15   While the scenario **NHSH** (orange line) also leads to a relatively evenly distributed zonal forcing in most latitudes, the total global forcing is clearly lower than in the case of **EQ**, **p2** and **p2w** scenarios (Table 1). In scenario **NH** (green line), the forcing is concentrated mainly to the northern hemisphere (-4.42 W/m^2). There is also moderate cooling effect in the southern hemisphere (-2.00 W/m^2).

20   Further insight into the different zonal and global radiative effects between the scenarios can be obtained from Figure 4, which shows the burden of stratospheric sulfate particles and the zonal distribution of the incoming solar radiation (shown in orange in the figure), in boreal winter (DJF) (fig4a) and summer (JJA) (fig4b). Sulfate burden and solar radiation are shown per meter in meridional direction. Thus the different length of the circumference along an individual latitude is taken account in the figure.

25

In the depicted seasons, the maximum solar radiation is received about 15 degrees south or north of the equator. Thus in scenario **EQ**, much of the zonal sulfate burden peak around the equator is not optimally located (black line) with respect to the incoming radiation. In addition, the meridional wind component over the equator (10° N – 10° S) in the stratosphere (20 - 25 km altitude) is on the average towards the north in the northern autumn and towards the south in the northern spring. Thus,

30   there is more sulfate in scenario **EQ** in the midlatitudes of the winter hemisphere, which gets significantly less solar radiation than the summer hemisphere. Thus, when the sulfate particles are concentrated to the winter hemisphere, they reflect less solar radiation making solar radiation management less efficient. On the other hand, in the **p2** scenario, the maximum of zonal mean sulfur burden is roughly at the same latitudes as the maximum solar radiation and, compared to scenario **EQ**, more sulfate is in the summer hemisphere. This leads to a larger radiative effect in scenario **p2** than in scenario **EQ** during the summer months

and but also to a smaller radiative effect in the winter months, as can be seen Figures 4c and d. Compared to scenario **EQ**, the total sky SW radiative forcing in scenario **p2** is 15% larger in the boreal summer months and 15% smaller in the winter months in the northern hemisphere. The difference can be seen especially in high latitudes (north of 50° N), where the mean radiative forcing is 23% larger in **p2** than in **EQ** in June-July-August (not shown). On the other hand, compared to scenario **EQ**, scenario **p2w** leads to 17% and 14% larger radiative forcing in the summer months over the northern and southern hemispheres, respectively. In winter months the radiative forcing is -14% and -16% lower in the northern and southern hemisphere respectively compared to scenario **EQ**.

3.2 Temperature and precipitation change - results of MPI-ESM simulations

In this section we investigate how the aerosol radiative effects simulated for the different injection scenarios in sect. 3.1 translate to global and regional climate impacts. The mean values for different scenarios were derived from ensembles of 3 simulations.

3.2.1 The global mean temperature and precipitation response

In SRM scenarios (**EQ**, **NH**, **NHSH**, **p2** and **p2w**), stratospheric sulfur injections are started at the full force (5 Tg(S)/yr) in year 2020 and suspended in year 2070. Compared to the global mean 2-meter temperature without SRM (**RCP45**), all scenarios lead to fast and relatively similar global mean cooling after the injections were started (fig5a). After that, the climate warms quickly due to the increased greenhouse gas concentration in RCP4.5. In **RCP45** scenario, between years 2060-2070 the global 2-meter temperature is 1.18 K warmer compared to years 2010-2020. Compared to **RCP45**, the global mean temperature is -1.27, -1.13, -1.21, -1.34 and -1.29 K cooler in scenarios **EQ**, **NH**, **NHSH**, **p2**, and **p2w** (not shown in the figure 5) between 2060-2070. Thus, the global mean temperature is close the value during the 2010s. Scenario **p2** leads to the largest global mean cooling which is slightly larger (4%) than in **EQ** as was expected based on simulations with ECHAM-HAMMOZ. Because SRM is turned on abruptly at full force in 2020, it would lead to a fast cooling. In the real world this kind of action is unlikely but based on the simulations plausible if needed for example prevent climate warming emergency (Kravitz et al., 2011).

After the very fast cooling in SRM scenarios, climate starts to warm slowly when as the aerosol reaches its maximum cooling effect and the GHG concentration in the atmosphere continues to increase. It is notable that even though this GHG induced warming effect is similar in all SRM scenarios, the warming rate is clearly slower than in RCP4.5. Between years from 2030 to 2070 warming rate is 1.95 K / 100 yr in **RCP45** scenario, but in scenario **EQ** the warming rate is reduced to 1.25 K / 100 yr. As the amount of injected sulfur does not change, the direct cooling effect of stratospheric sulfate particles does not increase during the years 2030-2070. However ocean reacts slowly to the abrupt changes in radiation and the changes in the atmospheric temperature (Giorgetta et al., 2013). Thus oceans are cooling in the beginning of SRM simulations which leads to slower warming compared to RCP4.5. Also the climate feedbacks and especially changes in ice albedo could slow down warming.

Ice area and thus albedo is clearly higher in all of the SRM scenarios before suspending than beginning of the simulation even though global mean temperature is at the same level. Adding to this, the climate system response is asymmetric to the increase or decrease of forcings (Schaller et al., 2014). It has been shown that there is a slow decrease in temperature still decades after a decrease in shortwave radiation (Schaller et al., 2014). Similar behavior of the global mean temperature in G4 scenario was observed also by Kashimura et al. (2016).

After the SRM is suspended in 2070 there is a very fast warming, called the termination effect of geoengineering (Jones et al., 2013). This warming is of the same magnitude as the cooling immediately after the sulfur injection is started. Thus, after the SRM is suspended, the climate remains significantly cooler for decades. If we make an assumption that the climate would warm after year 2020 at warming rate calculated from **EQ** from year 2030 to 2070 (blue dashed line in fig6a), the global temperature would be at the same level after 2070 than it is in SRM scenarios followed years after suspended sulfur injections. All of the SRM scenarios start to reach the temperature of **RCP45** a year after the suspension of SRM. However, up to the end of the simulation (years 2090-2099) the climate is still (0.17– 0.21) K cooler in SRM scenarios than **RCP45**. In a multimodel experiment, Jones et al., (2013) studied the termination effect in GeoMIP G2 scenario, where the forcing from 1%/yr increase in atmospheric CO_2 concentration was compensated decreasing the solar constant and the SRM was suspended, similarly to this study, in 2070. Some of the models shows still cooler climate compared to the RCP4.5 scenario in year 2100, but in MPI-ESM temperatures were at the same level in both G2 and RCP4.5 scenarios. However in here, in scenarios which were based on the G4 scenario with 5 Tg(S)/yr injections, climate was clearly over cooled before SRM was suspended compared to years before SRM when G2 temperatures has been kept same. Thus in scenarios here, oceans heat uptake is reduced more than in G2. Kashimura et al. (2016) studied G4 scenario in several models. Most of the models show similar behavior after suspending SRM as seen here. However, here the amount of injected sulfur was two times as large as Kashimura et al. (2016).

Compensating the GHG induced global warming using SRM leads to a reduction in the global mean precipitation (Kravitz et al., 2013b; Ferraro and Griffiths, 2016). This is also supported by our simulations. Immediately after the injection has been started, the global mean precipitation falls clearly under the level of year 2010 as can see in figure 5b. After few years, the global mean precipitation starts to increase slowly (0.048 mm/day/100yr in scenario **EQ** between years from 2040 to 2069). Change rate of precipitation is clearly smaller than in **RCP45** scenario (0.08 mm/day/100yr).

Between the years from 2060-2070, there is significantly less precipitation in all SRM scenarios than in 2010, even though temperatures are at the same level. Compared to years 2010 - 2020 the global mean precipitation has been changed by +0.044, -0.051, -0.036, -0.043 and -0.054 mm/day in **RCP45**, **EQ**, **NH**, **NHSH** and p2, respectively. Precipitation is thus more affected by the SRM than CO_2. There are mainly two causes for the changes in the global mean precipitation. One cause is the temperature change (Bony et al., 2013; Ferraro et al., 2014; Kravitz et al., 2013b) which inflicts a feedback response due to the increased humidity in the atmosphere. The second mechanism is the temperature independent atmospheric forcing (the

change in the radiation between the surface and the top of the atmosphere) (Ferraro et al., 2014; Ferraro and Griffiths 2016). This is the rapid adjustment which occurs in a short timescale, when the change in the radiative balance is compensated by the changes in latent and sensible heat flux (Bala et al., 2008). Increased CO_2 concentration in the atmosphere produces the temperature-independent forcing and a decrease in precipitation. This is because CO_2 affects the LW radiation in the whole

5   troposphere. However, when the climate warms, water vapor concentration is increased in the atmosphere. This increase would lead to an increase in precipitation which exceeds the decrease in precipitation due to the GHG radiative forcing. In SRM scenarios the GHG induced warming from 2010 (slow response) is roughly compensated between the years 2060-2070 thus counterbalancing the temperature-dependent increase in precipitation. However the temperature independent fast response (decrease in precipitation) due to the increased CO_2 concentration remains and is further amplified by the aerosol radiative

10   effects. Aerosol particles both absorb radiation (which is then emitted as LW radiation) and they reduce the SW radiation at surface. These effects lead to a drier climate (Ferraro and Griffiths 2016).

3.2.2 Spatial pattern of temperature and precipitation responses

Next we concentrate on the regional climate impacts between years 2060-2070 before SRM is suspended and where the global mean temperature does not change significantly. It has been suggested that global warming would lead to warmer climate in

15   the arctic and high latitudes than low latitudes (Stocker et al., 2013). In our simulations there is over 2 degrees warming in the arctic area between the years 2060-2070 compared to the 2010s temperatures in the **RCP45** scenario (fig 6a). Together with relatively uniform reduction in SW radiation (reduction in solar constant), it has been shown to lead to warming in the high latitudes and cooling at the low latitudes (Kravitz et al., 2013c; Schmidt et al., 2012). Our results show that there will be cooling in the tropics and small warming at the midlatitudes in scenario **EQ** as indicated by earlier studies. However there is

20   also cooling at the arctic (fig6b). This might be because climate in the northern hemisphere will still be cooler in 2060-2070 than reference years (2010-2020). The arctic sea ice will respond strongly to temperature changes and the ice cover area is 8% larger in **EQ** between years 2060-2070 than in the beginning of the simulation. In addition, this area is significantly warmer in one of the ensemble members between years 2010 – 2020 compared to other simulations. Overall the size of the area of this arctic cooling region is small compared regions in midlatitudes which have been warmed after the 2010s.

25

Fig 6 c-f shows the difference between the alternative injection and scenario **EQ**. In scenarios **p2** and **p2w** there is less radiative forcing at the tropics and larger radiative effect in higher latitudes compared to scenario **EQ**. Although this does not translate directly to differences in the regional temperature near the surface as they are affected by other factors in the climate (Stocker et al., 2013), both **p2** and **p2w** show statistically significant cooling at the midlatitudes at North America and Northern Pacific

30   when compared to **EQ**. In these areas scenario **EQ** leads to warming from years 2010-2020. As expected, the equator was warmer in **p2w** compared to scenario **EQ**.

If stratospheric sulfur injections were concentrated to the northern hemisphere (**NH**) it would lead to a significant cooling in northern midlatitudes compared to injections to the equator (**EQ**). Nevertheless, polar region over Eurasia is not cooler compared to scenario **EQ**. Arctic area is warmer especially in boreal winter, when the cooling effect of the particles from the northern hemisphere injections is weak (fig7a). On other hand in **EQ** scenario the climate will be generally cooler and thus climate also is cooler at the polar regions over Eurasia compared to scenario **NH**. Thus based on these results, for example the melting of the arctic ice cover is prevented more efficiently by injecting sulfur to the equator than concentrating the injections only to the northern hemisphere which would cool area mainly in boreal summer. In scenario **NHSH** the northern hemisphere is generally cooled less by sulfate aerosols and thus polar region is even warmer compared to **NH** and **EQ**. In addition in scenario **NHSH**, the tropical region is warmer compared to scenario **EQ** as was expected based on fig 3.

Radiative forcing simulated and calculated by ECHAM-HAMMOZ (see Sect. 3.1) showed that scenarios **p2** and **p2w** lead to amplified seasonal effect of radiative forcing in hemisphere compared to **EQ** (fig4c,d). Thus **p2w** leads to 0.05 K cooler climate in northern hemisphere summer (JJA, fig7b) and 0.05 K cooler in southern hemisphere summer (DJF, fig7a) than **EQ**. It is noteworthy that strong radiative forcing does not translate to large changes in temperature. For example, if we compare the cooling in different scenarios to the scenario without SRM (**RCP45**), compared to the simulation **EQ** the summer time forging in scenario **p2w** is 17% stronger in the northern hemisphere and 14% in the southern hemisphere. However, scenario **p2w** leads to only 3% cooler climate in the northern and southern hemisphere summers than scenario **EQ**.

GHG induced climate warming would increase global mean precipitation as was seen in chapter 3.2.1. Figure 8a shows yearly mean increase in precipitation is largest at the equatorial Pacific. This is in good agreement with intergovernmental panel on climate change (IPCC) estimations (Stocker et al., 2013). These regions correspond to the spatial maximum of sea surface temperature (SST) warming at equatorial Pacific (Xie et al., 2010). Similarly SST warming exceeds the mean SST warming at northern Pacific and Atlantic where precipitation has increased. It has been also shown that P – E (Precipitation – Evaporations) will become more intense (Seager et al., 2010) which will cause wet areas to become wetter but also drying in the subtropical regions such as Mediterranean, Southern part of Africa and Australia. In **EQ** scenario precipitation is decreased in the equatorial Pacific where SST is mainly decreased from the years 2010-2020 (fig8b). The only exception is the eastern part of equatorial Pacific where there has been slight warming in SST which is resulted increased precipitation. In addition in **EQ** scenario, P-E is not significantly changed in subtropical regions and the precipitation is at same level as in 2010s. However there is clearly less precipitation in northern part of South-America in both scenarios **RCP45** and **EQ**. This might be due the change in the Atlantic SST gradient (similar in **RCP45** and **EQ**) and influence to ITCZ (Haywood et al., 2013). This will lead to reduced moisture which is transported from Atlantic. If sulfur is injected to the northern hemisphere (scenario **NH**), the change in Atlantic SST gradient is opposite compared to scenario **RCP45** and **EQ** which lead to increased precipitation in northern South-America and drying of Sahel (fig8c).

Overall regional precipitation changes between studied injection scenarios are not statistically significant. All alternative injection scenarios lead to slight decrease in Atlantic SST gradient which lead to drier Sahel but increased precipitation in southern equatorial Atlantic compared to scenario **EQ**. In Addition equatorial Pacific SST is decreased relatively more compared to scenario **EQ** which lead to a larger reduction in precipitation especially in scenarios **p2** and **p2w**. Seasonal zonal mean precipitation response is slightly different in scenarios **EQ** and **p2** (fig7c,d).

At JJA there is relatively large difference in zonal mean anomalies of precipitation at tropics between the **EQ** and **p2** scenarios (Fig 7c,d). In both case there will be less precipitation compared to the reference years (2010-2020), but decrease is clearly larger in northern low latitudes in **p2** than **EQ** and opposite at southern low latitudes. Sobel and Camargo 2011 showed that an increase in the summer hemisphere SST and a decrease in the winter hemisphere SST lead to strengthening of easterly trade winds in the winter subtropics and weakening in the summer subtropics. This is further associated to Hadley cell circulation and ITCZ which affect strongly to the precipitation response in Tropics. As has shown **p2** lead to larger cooling effect at the summer hemisphere and weaker at the winter hemisphere than scenario **EQ**, which might explain different seasonal precipitation responses at tropics.

4. Summary and conclusions

Here we used an atmosphere-only GCM coupled to an aerosol model to simulate the radiative properties of different stratospheric sulfur injection strategies than injecting sulfur only to equator. In the second part of the study we studied how radiative forcings from different injection scenarios translate to temperature and precipitation impacts by using Max Planck Institute Earth System Model. We estimated how different emission areas of stratospheric sulfur could be used to optimize the aerosol radiative forcing as well as how the decrease in the meridional temperature gradient typical for SRM scenarios could be minimized.

In all simulated scenarios, 5 Tg(S)/yr of SO_2 was injected to 20° latitude wide band (2 bands in **NHSH**) and the resulting radiative and climate effects were compared to those in a scenario where sulfur is injected only equator. According our aerosol microphysical simulations by GCM, it would be possible to maintain as large global cooling effect as by injecting sulfur only in the equator while concentrating the cooling effect more to the midlatitudes than tropics. This could be achieved if the sulfur injection area is changed during the year. Such a scenario was **p2w** where the injection area changed from its northernmost position (40° N - 20° N) at April to the southernmost position (20° S - 40° S) at October. In this scenario the mean radiative forcing was 27% smaller between 20° N and 20° S latitudes and outside this area 15% larger than in the simulation **EQ** which assumed fixed injection area over the equator (10° S - 10° N). If the injection area is changed similarly but between 30° N and 30° S latitudes (**p2**), the global mean shortwave radiative forcing was 3% larger than injecting sulfur only equator (**EQ**). More

of the injected sulfur was located at the summer hemisphere in **p2** compared to **EQ**. Thus the radiative forcing was relatively larger (15%) in the summer hemispheres and relatively weaker (15%) at winter hemispheres compared to **EQ**.

Based on this study effectiveness of seasonally changed injection area depends on seasonality of (intensity) solar radiation, oxidation of SO_2 (which depends on availability of OH) and lifetime of sulfate particles. It is noteworthy that our simulations indicate that the efficiency of the aerosol radiative forcing in Scenario **EQ** was not significantly increased in any of our simulations.

Scenarios simulated by ESM were based on GeoMIP G4 scenarios, where the aerosols injection (5 Tg(S)/yr instead of 2.5 in G4) is been started at full force in 2020 and then suspended in 2070. Solar radiation management scenarios studied here lead to a cooling of 1.13 – 1.34 K. Compared to **RCP45** the warming rate between years 2030-2070 was reduced from 1.95 K / 100 yr to 1.25 K / 100 yr in SRM scenarios due to the ocean cooling caused by aerosol radiative effect. This highlights the role of feedbacks and ocean temperature which reacts slowly to the radiation changes in the atmosphere.

ESM simulations also showed that by changing injection area during the year, it would be possible to get more cooling to the midlatitudes and less cooling at tropics compared to injections only to the equator. This can be also achieved by injecting sulfur only to 30° N - 10° N and 10° S - 30° S latitudes (**NHSH**). However, then the climate cooling was 15% smaller than in scenarios where the injection area was varying during the year. These injection strategies could be used to avoid reduction of meridional temperature gradient, which has been seen in many previous studies where SRM have been investigated. Results of this study also indicate that the melting of arctic sea ice is more efficiently prevented by tropical injections than injection only to northern hemisphere (30° N - 10° N, scenario **NH**), in which case the cooling effect at boreal winter is relatively weak.

The global mean precipitation was clearly decreased in all of our SRM simulations even the temperature changes was roughly compensated. This is consistent with earlier studies. When looking seasonal values, different injection scenarios led to different results especially at the tropics. However modelling precipitation changes is very uncertain and making valid conclusions about regional precipitation by using global model is challenging.

Forschungszentrum Jülich, University of Oxford and the Finnish Meteorological Institute and managed by the Center of Climate Systems Modeling (C2SM) at ETHZ

References

Aswathy, V. N., Boucher, O., Quaas, M., Niemeier, U., Muri, H., Mülmenstädt, J., and Quaas, J.: Climate extremes in multi-model simulations of stratospheric aerosol and marine cloud brightening climate engineering, Atmos. Chem. Phys., 15, 9593-9610, doi:10.5194/acp-15-9593-2015, 2015.

Bala G., Duffy P. B., Taylor K. E.: Impact of geoengineering schemes on the global hydrological cycle. Proc Natl Acad Sci USA 105:7664-7669. doi:10.1073/pnas.0711648105, 2008

Bony, S., Bellon, G., Klocke, D., Sherwood, S., Fermepin, S., and Denvil, S.: Robust direct effect of carbon dioxide on tropical circulation and regional precipitation, Nat. Geosci., 6, 447-451, 2013.

Bergman, T., Kerminen, V.-M., Korhonen, H., Lehtinen, K. J., Makkonen, R., Arola, A., Mielonen, T., Romakkaniemi, S., Kulmala, M., and Kokkola, H.: Evaluation of the sectional aerosol microphysics module SALSA implementation in ECHAM5-HAM aerosol-climate model, Geosci. Model Dev., 5, 845–868, doi:10.5194/gmd-5-845-2012, 2012.

Dentener, F., Kinne, S., Bond, T., Boucher, O., Cofala, J., Generoso, S., Ginoux, P., Gong, S., Hoelzemann, J. J., Ito, A., Marelli, L., Penner, J. E., Putaud, J.-P., Textor, C., Schulz, M., van der Werf, G. R., and Wilson, J.: Emissions of primary aerosol and precursor gases in the years 2000 and 1750 prescribed data-sets for AeroCom, Atmos. Chem. Phys., 6, 4321–4344, doi:10.5194/acp-6-4321-2006, 2006.

English, J. M., Toon, O. B., and Mills, M. J.: Microphysical simulations of sulfur burdens from stratospheric sulfur geoengineering, Atmos. Chem. Phys., 12, 4775-4793, doi:10.5194/acp-12-4775-2012, 2012.

Ferraro, A. J., Highwood, E. J., and Charlton-Perez, A. J.: Weakened tropical circulation and reduced precipitation in response to geoengineering, Environ. Res. Lett., 9, doi:10.1088/17489326/9/1/014001, 2014.

Ferraro., A. J. and Griffiths, H. G.: Quantifying the temperature-independent effect of stratospheric aerosol geoengineering on global-mean precipitation in a multi-model ensemble, Environ. Res. Lett. 11 034012, doi.org/10.1088/1748-9326/11/3/034012, 2016.

Haywood, J. M., Jones, A., Bellouin, N., Stephenson, D.: Asymmetric forcing from stratospheric aerosols impacts Sahelian rainfall, Nature Clim. Change, 3, 660–665, doi:10.1038/nclimate1857, 2013.

Heckendorn P, Weisenstein D, Fueglistaler S, Luo B P, Rozanov E, Schraner M, Thomason L W and Peter T. The impact of geoengineering aerosols on stratospheric temperature and ozone Environ. Res. Lett. 4, 045108, 2009.

Giorgetta, M., Jungclaus, J., Reick, C. H., Legutke, S., Bader, J., Böttinger, M., Brovkin, V., Crueger, T., Esch, M., Fieg, K., Glushak, K., Gayler, V., Haak, H., Hollweg, H.-D., Ilyina, T., Kinne, S., Kornblueh, L., Matei, D., Mauritsen, T., Mikolajewicz, U., Mueller, W., Notz, D., Pithan, F., Raddatz, T., Rast, S., Redler, R., Roeckner, E., Schmidt, H., Schnur, R., Segschneider, J., Six, K. D., Stockhause, M., Timmreck, C., Wegner, J., Widmann, H., Wieners, K.-H., Claussen, M.,

Marotzke, J., and Stevens, B.: Climate and carbon cycle changes from 1850 to 2100 in MPI-ESM simulations for the coupled model intercomparison project phase 5, J. Adv. Model. Earth Syst., 5, 572–597, doi:10.1002/jame.20038, 2013.

Jones, A., Haywood, J., Boucher, O., Kravitz, B., and Robock, A.: Geoengineering by stratospheric SO_2 injection: results from the Met Office HadGEM2 climate model and comparison with the Goddard Institute for Space Studies ModelE, Atmos. Chem.

5   Phys., 10, 5999-6006, doi:10.5194/acp-10-5999-2010, 2010.

Ilyina, T., Six, K. D., Segschneider, J., Maier-Reimer, E., Li, H., and& Nunez-Riboni, I.. Global ocean biogeochemistry model HAMOCC: Model architecture and performance as component of the MPI-Earth System Model in different CMIP5 experimental realizations.J. Adv. Model. Earth Syst. , 5, 287-315. doi:10.1029/2012MS000178, 2013.

Jones, A., Haywood, J. M., Alterskjær, K., Boucher, O., Cole, J. N. S., Curry, C. L., Irvine, P. J., Ji, D., Kravitz, B.,

10   Kristjánsson, J. E.., Moore, J. C., Niemeier, U., Robock, R., Schmidt, H. Singh, H., Tilmes, S., Watanabe, S. and Yoon, J.H.; The impact of abrupt suspension of solar radiation management (termination effect) in experiment G2 of the Geoengineering Model Intercomparison Project (GeoMIP), Journal of Geophysical Research, 118(17), 9743-9752, doi:10.1002/jgrd.50762, 2013.

Jones, A. C., Haywood, J. M., and Jones, A.: Climatic impacts of stratospheric geoengineering with sulfate, black carbon and

15   titania injection, Atmos. Chem. Phys., 16, 2843-2862, doi:10.5194/acp-16-2843-2016, 2016.

Kashimura, H., Abe, M., Watanabe, S., Sekiya, T., Ji, D., Moore, J. C., Cole, J. N. S., and Kravitz, B.: Shortwave radiative forcing and feedback to the surface by sulphate geoengineering: Analysis of the Geoengineering Model Intercomparison Project G4 scenario, Atmos. Chem. Phys. Discuss., doi:10.5194/acp-2016-711, in review, 2016.

Jungclaus, J. H., Fischer, N., Haak, H., Lohmann, K., Marotzke, J., Matei, D., Mikolajewicz, U., Notz, D., & von Storch, J.-

20   S.. Characteristics of the ocean simulations in MPIOM, the ocean component of the MPI Earth System Model. J. Adv. Model. Earth Syst. , 5, 422-446. doi:10.1002/jame.20023, 2013.

Kinne, S., D. O'Donnell, D., P. Stier, P., S. Kloster, S., K. Zhang, K., H. Schmidt, H., S. Rast, S., M. Giorgetta, M., T. F. Eck, T.F and B. Stevens, B., MAC-v1: A new global aerosol climatology for climate studies, J. Adv. Model. Earth Syst., 5, 704–740, doi:10.1002/jame.20035, 2013.

25   Kokkola, H., Korhonen, H., Lehtinen, K. E. J., Makkonen, R., Asmi, A., Järvenoja, S., Anttila, T., Partanen, A.-I., Kulmala, M., Järvinen, H., Laaksonen, A., and Kerminen, V.-M.: SALSA – a Sectional Aerosol module for Large Scale Applications, Atmos. Chem. Phys., 8, 2469–2483, doi: 10.5194/acp-8-2469-2008, 2008.

Kravitz, B., Robock, A., Boucher, O., Schmidt, H.,Taylor K. E., Stenchikov, G. and Schulz M.: The Geoengineering Model Intercomparison Project (GeoMIP), Atmospheric Science Letters, 12, 162-167, doi:10.1002/asl.316, 2011.

30   Kravitz, B., Robock, A., Forster, P. M., Haywood, J. M., Lawrence M. G., and Schmidt, H.: An overview of the Geoengineering Model Intercomparison Project (GeoMIP), Journal of Geophysical Research, 118, 13103-13107, doi:10.1002/2013JD020569, 2013a.

Kravitz, B.., Rasch, P. J., Forster, P. M., Andrews, T., Cole, J. N. S., Irvine, P. J., Ji, D., Kristjánsson,J. E., Moore, J. C., Muri, H., Niemeier, U., Robock, A., Singh, B., Tilmes, S., Watanabe, S., and Yoon, J.-H.: , An energetic perspective on hydrological

16

cycle changes in the Geoengineering Model Intercomparison Project, J. Geophys. Res. Atmos., 118, 13,087–13,102, doi: 10.1002/2013JD020502, 2013b.

Kravitz, B., Caldeira, K., Boucher, O., Robock, A., Rasch, P. J., Alterskjær, K., Karam, D., B., Cole, J. N. S., Curry, C. L., Haywood, J. M., Irvine, P. J., Ji, D., Jones, A.,Kristjánsson, J. E., Lunt, D. J., Moore, J. C., Niemeier, U., Schmidt, H., Schulz, M., Singh, B., Tilmes, S., Watanabe, S., Yang, S., and Yoon, J.-H.:, Climate model response from the Geoengineering Model Intercomparison Project (GeoMIP), J. Geophys. Res. Atmos., 118, 8320–8332, doi:10.1002/jgrd.50646, 2013c.

Laakso, A., Kokkola, H., Partanen, A.-I., Niemeier, U., Timmreck, C., Lehtinen, K. E. J., Hakkarainen, H., and Korhonen, H.: Radiative and climate impacts of a large volcanic eruption during stratospheric sulfur geoengineering, Atmos. Chem. Phys., 16, 305-323, doi:10.5194/acp-16-305-2016, 2016.

MacMartin, D. G., Keith, D. W., Kravitz, B., and Caldeira, K.: Management of trade-offs in geoengineering through optimal choice of non-uniform radiative forcing, Nat. Clim. Change, 3, 365–368, doi:10.1038/nclimate1722, 2012.

McCusker, K. E., Battisti, D. S. and Bitz, C. M.: The climate response to stratospheric sulfate injections and implications for addressing climate emergencies, J. Clim., 25(9), 3096–3116, doi:10.1175/JCLI-D-11-00183.1, 2012.

Modak, A. and Bala, G.: Sensitivity of simulated climate to latitudinal distribution of solar insolation reduction in solar radiation management, Atmos. Chem. Phys., 14, 7769-7779, doi:10.5194/acp-14-7769-2014, 2014.

Moss, R. H., Edmonds, J. A., Hibbard, K. A., Manning, M. R., Rose, S. K., van Vuuren, D. P., Carter, T. R., Emori, S., Kainuma, M., Kram, T., Meehl, G. A., Mitchell, J. F. B., Nakicenovic, N., Riahi, K., Smith, S. J., Stouffer, R. J., Thomson, A. M., Weyant, J. P., and Wilbanks, T. J.: The next generation of scenarios for climate change research and assessment, Nature, 463, 747–756, doi:10.1038/nature08823, 2010.

Niemeier, U., Schmidt, H., and Timmreck, C.: The dependency of geoengineered sulfate aerosol on the emission strategy, Atmos. Sci. Lett., 12, 189–194, doi: 10.1002/asl.304, 2011.

Pierce, J. R.; Weisenstein, D. K.; Heckendorn, P.; Peter, T.; Keith, D. W.: Efficient formation of stratospheric aerosol for climate engineering by emission of condensable vapor from aircraft, Geophysical Research Letters, 37, doi:10.1029/2010GL043975, 2010.

Pope, F. D., Braesicke, P., Grainger, R. G., Kalberer, M., Watson, I. M., Davidson, P. J., and Cox, R. A.: Stratospheric aerosol particles and solar-radiation management, Nature Clim. Change, 2, 713-719, doi:10.1038/nclimate1528, 2012.

Reick, C., T. Raddatz, T. V., Brovkin, V. and V. Gayler, V., The representation of natural and anthropogenic land cover change in MPI-ESM, J. Adv. Model. Earth Syst., 5, 459-482, doi:10.1002/jame.20022, 2013.

Robock, A., Oman, L., and Stenchikov G. L.: Regional climate responses to geoengineering with tropical and Arctic SO 2 injections, J. Geophys. Res., 113, D16101, doi:10.1029/2008JD010050, 2008.

Royal Society: Geoengineering the climate - Science, governance and uncertainty, RS Policy document 10/09, ISBN: 978-0-85403-773-5, 2009.

Schaller, N.,Sedlácek J., and Knutti R.: The asymmetry of the climate system's response to solar forcing changes and its implications for geoengineering scenarios, J. Geophys. Res. Atmos., 119, 5171–5184,doi:10.1002/2013JD021258, 2014.

Schmidt, H., Alterskjær, K., Bou Karam, D., Boucher, O., Jones, A., Kristjánsson, J. E., Niemeier, U., Schulz, M., Aaheim, A., Benduhn, F., Lawrence, M., and Timmreck, C.: Solar irradiance reduction to counteract radiative forcing from a quadrupling of CO_2 : climate responses simulated by four earth system models, Earth Syst. Dynam., 3, 63-78, doi:10.5194/esd-3-63-2012, 2012.

5   Seager, R., Naik, N., Vecchi, G. A.:Thermodynamic and dynamic mechanisms for large-scale changes in the hydrological cycle in response to global warming. J Clim 23(17):4651–4668. doi: 10.1175/2010JCLI3655.1, 2010.

Sobel, A. H. and Camargo, S. J.: Projected future changes in tropical summer climate. Journal of Climate, 24, 473-487, 2011.

Stocker, T., Qin, D., Plattner, G.-K., Tignor, M., Allen, S., Boschung, J., Nauels, A., Xia, Y., Bex, V., and Midgley, P.: The

10   Physical Science Basis. Working Group I Contribution to the Fifth Assessment Report of the Intergovernmental Panel on Climate Change. In IPCC, 2013: Climate Change 2013 . Cambridge University Press, Cambridge, United Kingdom and New York, NY, USA, 2013.

Stevens, B., Giorgetta, M., Esch, M., Mauritsen, T., Crueger, T., Rast, S., Salzmann, M., Schmidt, H., Bader, J., Block, K., Brokopf, R., Fast, I., Kinne, S., Kornblueh, L., Lohmann, U.,Pincus, R., Reichler, T., and Roeckner, E.: The atmospheric

15   component of the MPI-M Earth System Model: ECHAM6, J. Adv. Model. Earth Syst., 5, 1–27, doi:10.1002/jame.20015, 2013.

Taylor, K.E., Stouffer, R.J., Meehl G.A., A summary of the CMIP5 experiment design, World Climate Research Programme (WCRP), http://cmip-pcmdi.llnl.gov/cmip5/docs/Taylor_CMIP5_design.pdf

Timmreck, C., Graf, H.-F., Lorenz, S. J., Niemeier, U., Zanchettin, D., Matei, D., Jungclaus, J. H., and Crowley T. J.: Aerosol size confines climate response to volcanic super-eruptions (2010), Geophys. Res. Lett., 37, L24705, doi:

20   10.1029/2010GL045464, 2010.

Tilmes, S., Mills, M. J., Niemeier, U., Schmidt, H., Robock, A., Kravitz, B., Lamarque, J.-F., Pitari, G., and English, J. M.: A new Geoengineering Model Intercomparison Project (GeoMIP) experiment designed for climate and chemistry models, Geosci. Model Dev., 8, 43-49, doi:10.5194/gmd-8-43-2015, 2015.

Volodin, E. M., Kostrykin, S. V. and Ryaboshapko, A. G.: Climate response to aerosol injection at different stratospheric

25   locations. Atmosph. Sci. Lett., 12: 381–385. doi:10.1002/asl.351, 2013.

van Vuuren, D. P., Edmonds, J., Kainuma, M., Riahi, K., Thomson, A., Hibbard, K., Hurtt, G. C., Kram, T., Krey, V., Lamarque, J.-F., Masui, T., Meinshausen, M., Nakicenovic, N., Smith, S. J., and Rose, S. K.: The representative concentration pathways: an overview, Climatic Change, 109, 5–31, doi:10.1007/s10584-011-0148-z, 2011.

Xie, S., Deser, C., Vecchi, G., Ma, J., Teng, H. and Wittenberg, A.: Global Warming Pattern Formation: Sea Surface

30   Temperature and Rainfall. J. Climate, 23, 966–986, doi: 10.1175/2009JCLI3329.1, 2010.

Yu, X., Moore, J. C., Cui, X., Rinke, A., Ji, D., Kravitz, B., Yoon, J.-H.: Impacts, effectiveness and regional inequalities of the GeoMIP G1 to G4 solar radiation management scenarios. In: Global and Planetary Change. doi: 10.1016/j.gloplacha.2015.02.010, 2015.

Scenario	Strat. SO$_2$ burden Tg(S)	Strat. H$_2$SO$_4$ burden Tg(S)	All-sky SW forcing at TOA (W/m^2)
EQ	0.69	6.15	-3.72
NH	0.80	5.46	-3.21
NHSH	0.79	5.66	-3.30
p0	0.64	6.15	-3.67
p2	0.66	6.28	-3.82
p4	0.75	6.18	-3.74
p6	0.84	5.98	-3.58
p2w	0.68	6.29	-3.72

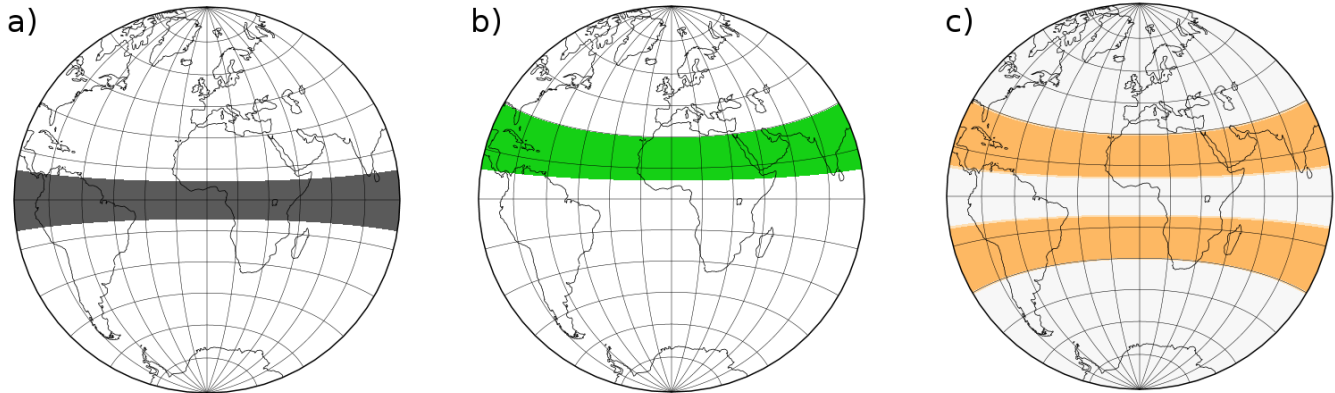Table 1. Five-year mean values of stratospheric sulfur dioxide and particulate sulfate burdens and the global shortwave (SW) all-sky forcing.

5

Figure 1. Injection areas in scenarios a) EQ, b) NH and c) NHSH
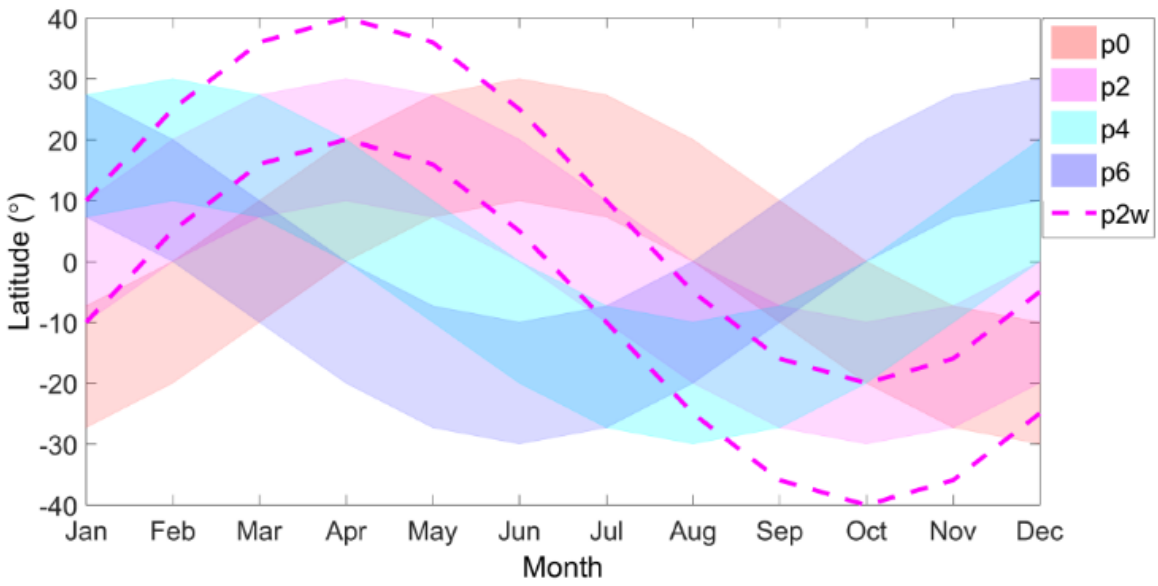
Figure 2. Seasonally changing injection areas in p0, p2, p4 and p6 scenarios
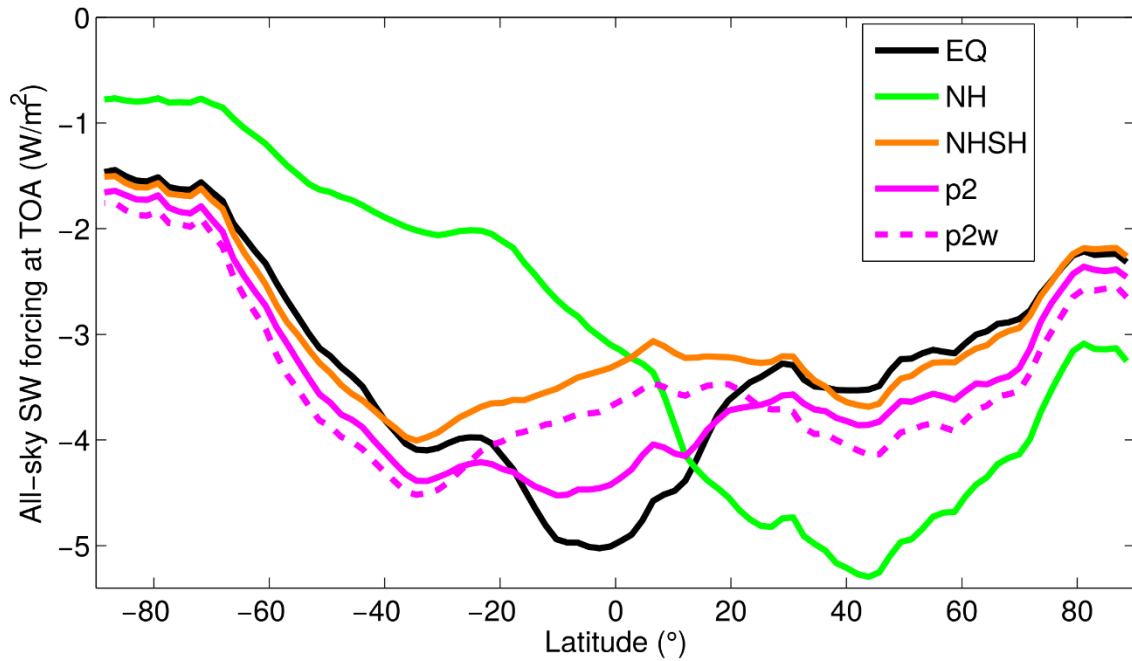
Figure 3. Five-year zonal means of all-sky shortwave radiative forcing in selected scenarios.
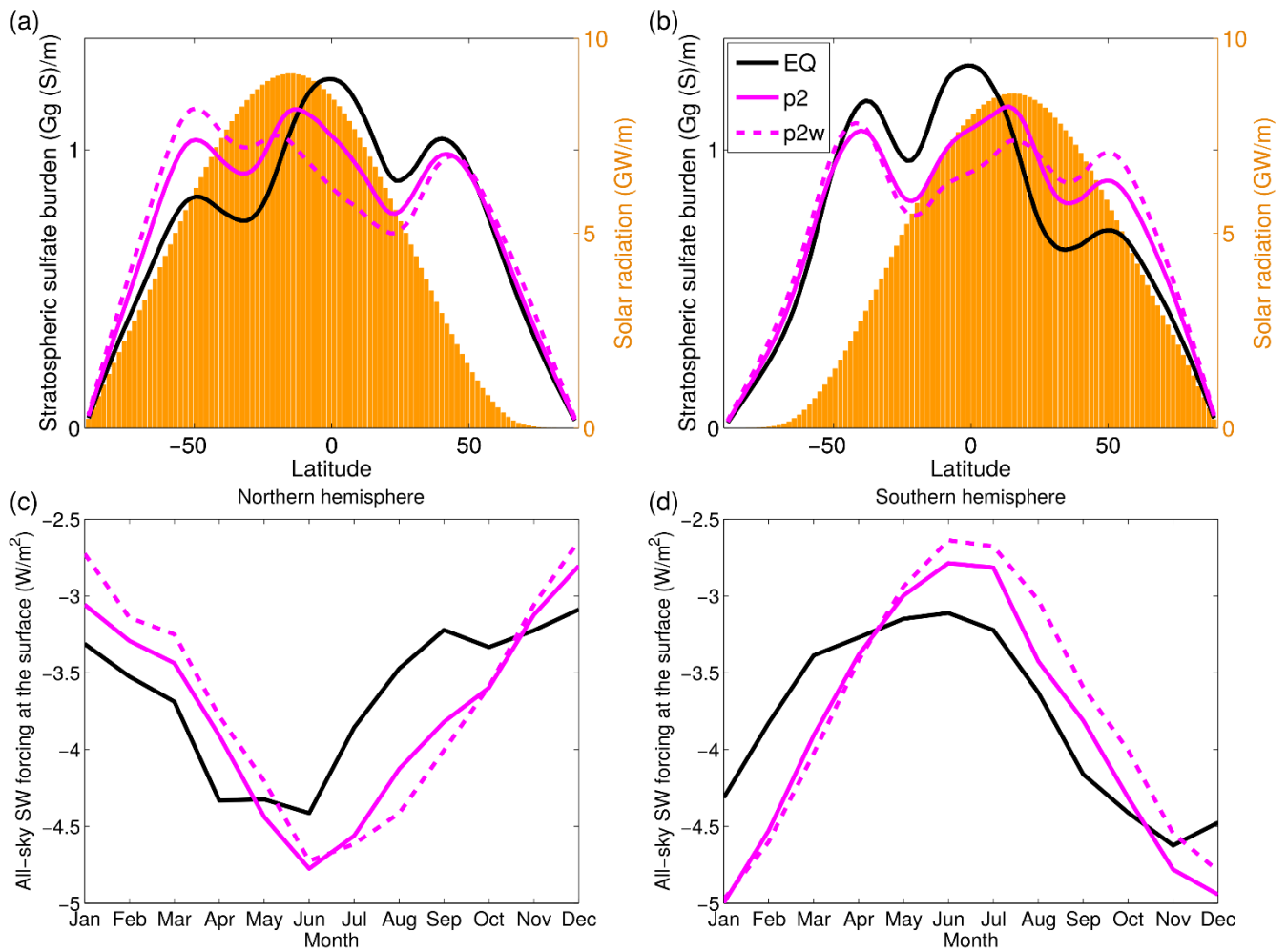
Figure 4. Zonal distribution of stratospheric particulate sulfate burden and zonally distributed incoming solar radiation in the a) December-January-February and b) June-July-August and the all sky shortwave radiative forcing at c) the northern hemisphere and d) the southern hemisphere. In a) and b) figures sulfate burden and solar radiation have shown per meridional meter.
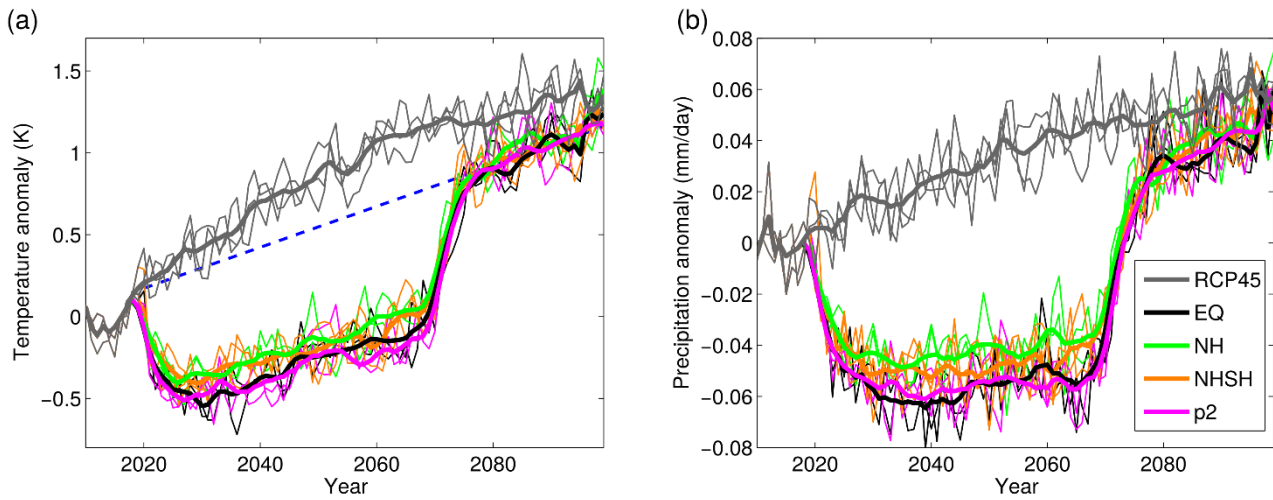
Figure 5. Global mean a) temperature, b) precipitation anomaly compared to the mean temperature at 2010s. The thick solid line shows the 5-year running ensemble mean values and each narrow line indicates the yearly mean values of one ensemble member. The blue dashed line shows the temperature after year 2020 according to mean warming rate in EQ between years 2030 and 2070.
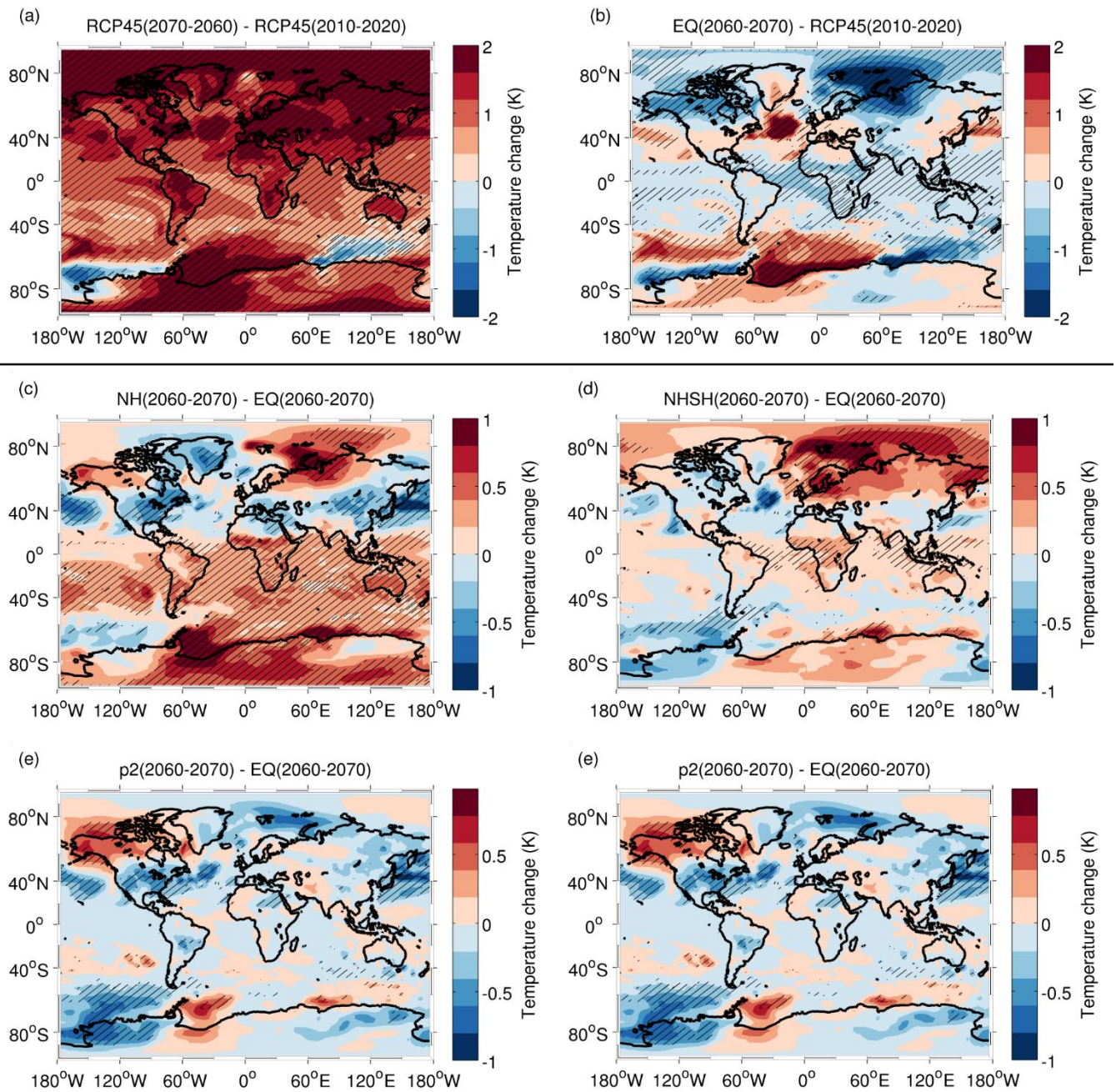
Figure 6. Temperature anomalies for a) RCP45, b) EQ, c) NH, d) NHSH, e) p2 and f) p2w. Anomalies in a) and b) are presented as a differences between years 2060-2070 and 2010-2020. Anomalies in c) d) e) and f) are presented as difference to EQ between years 2060-2070. Hatching indicates a regions where the change of temperature is statistically significant at 95% level.
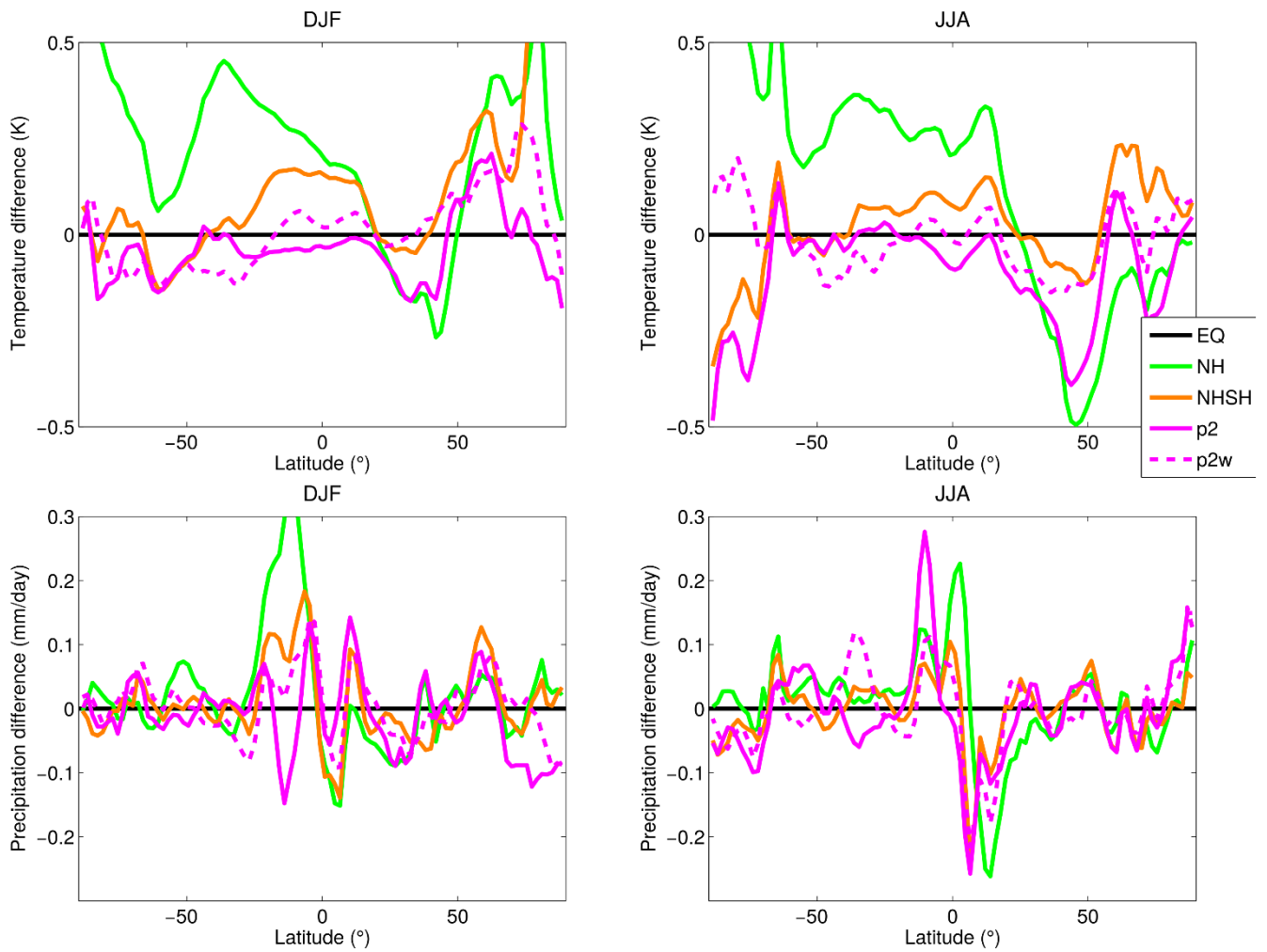
23

Figure 7. Zonal mean anomalies for the temperature in a) December-January-February and b) June-July-August and for precipitation in c) December-January-February d) June-July-August compared to scenario EQ.
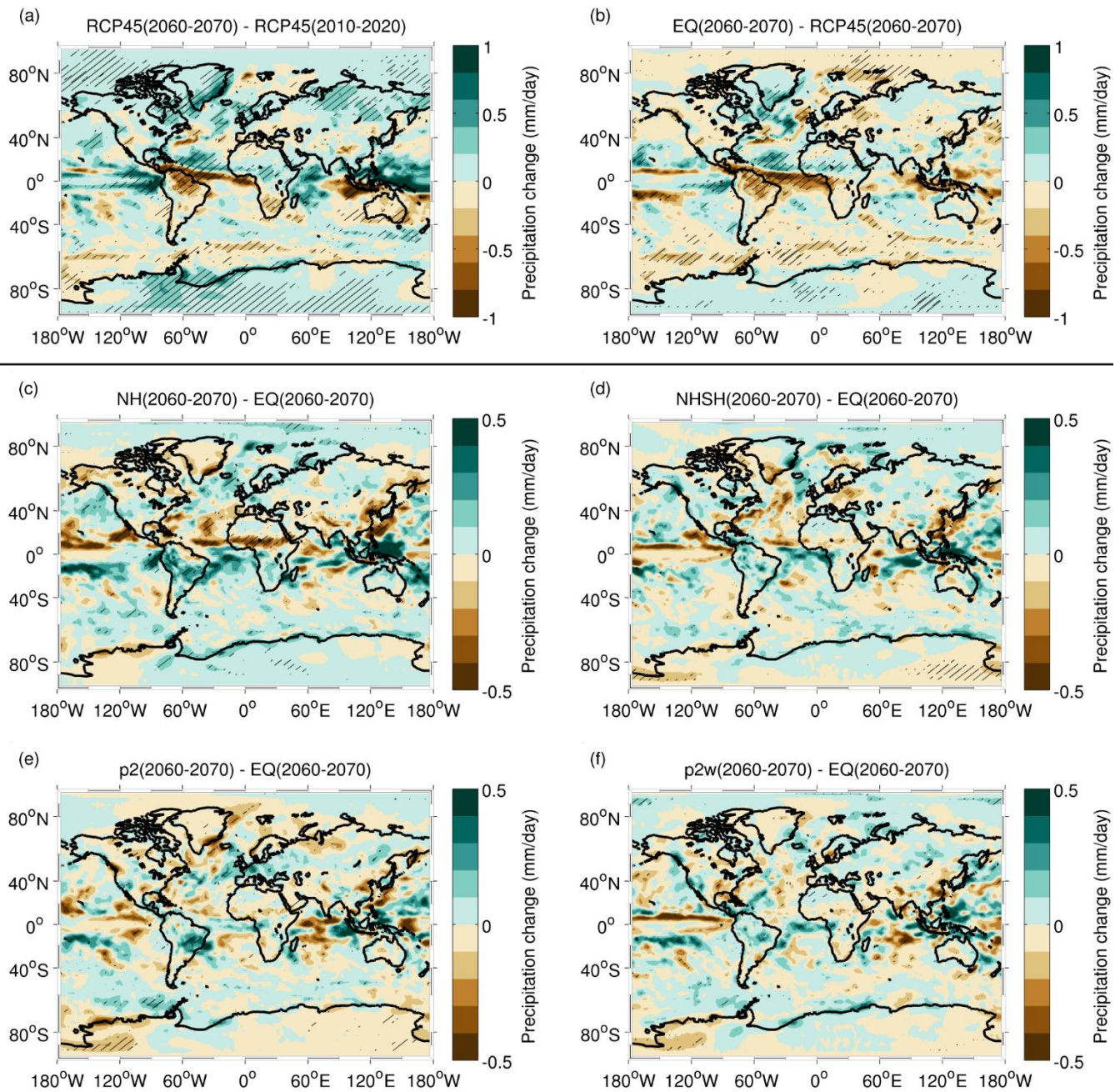
Figure 8. Precipitation anomalies for a) RCP45, b) EQ, c) NH, d) NHSH, e) p2 and f) p2w. Anomalies in a) and b) are presented as a differences between years 2060-2070 and 2010-2020. Anomalies in c) d) e) and f) are presented as difference to EQ between years 2060-2070. Hatching indicates a regions where the change of precipitation is statistically significant at 95% level.